




Cite this: *J. Mater. Chem. A*, 2018, 6, 19488

# Ni foam supported NiO nanosheets as high-performance free-standing electrodes for hybrid supercapacitors and Ni–Zn batteries†

Qiang Chen, Jiantao Li, Cong Liao, Guangwu Hu, Yulu Fu, Owusu Kwadwo Asare, Shu Shi,  Ziang Liu, Liang Zhou \* and Liqiang Mai \*

Herein, Ni foam (NF) supported NiO nanosheets with a NF@NiO core@shell structure have been synthesized by a facile etching-reoxidation method. The obtained NF@NiO can function as high-performance free-standing electrodes for both hybrid supercapacitors and Ni–Zn batteries. When employed as the cathode for hybrid supercapacitors, the NF@NiO exhibits a high areal capacitance of  $2.01 \text{ F cm}^{-2}$  at  $8 \text{ mA cm}^{-2}$ . By coupling with an FeOOH anode, the assembled NF@NiO//FeOOH asymmetric supercapacitor delivers a peak energy density of  $2.15 \text{ mW h cm}^{-3}$  and a peak power density of  $2.75 \text{ W cm}^{-3}$ . A rechargeable Ni–Zn battery is also assembled using NF@NiO as the cathode. The NF@NiO//Zn battery demonstrates a high maximum energy density ( $25.6 \mu\text{W h cm}^{-2}$ ) and an impressive power density ( $86.48 \text{ mW cm}^{-2}$ ) with remarkable cycling durability (84.7% capacity retention for 10 000 cycles). These features make the free-standing NF@NiO a promising candidate for electrochemical energy storage.

Received 4th August 2018  
Accepted 12th September 2018

DOI: 10.1039/c8ta07574c

rsc.li/materials-a

## Introduction

The rapid development of portable electronics calls for miniaturized energy storage devices with high energy/power density, long cycle life, excellent flexibility, and good safety.<sup>1–3</sup> Hybrid supercapacitors (HSCs) represent one of the most efficient energy storage devices because of their fast surface redox reactions, excellent cyclability, and high power density.<sup>4–6</sup> Transition metal oxides (TMOs) have been extensively investigated as hybrid supercapacitor materials due to their rich oxidation states.<sup>7–9</sup> Among various TMOs, Ni-based oxides have attracted great interest owing to their multiple merits of low cost, high theoretical capacitance, and good reversibility.<sup>10–12</sup> With intrinsically good safety, abundant resources, high capacity and output voltage ( $\sim 1.8 \text{ V}$ ), Ni–Zn batteries have been recognized as sustainable and promising alternatives to lithium-ion batteries.<sup>13–16</sup> Interestingly, Ni-based oxides have also been frequently studied as cathode materials for Ni–Zn batteries.<sup>17,18</sup> However, the Ni-based oxides often suffer from poor conductivity, limited electrochemical active sites, and insufficient stability.<sup>10,12,19</sup> To solve these issues, tremendous efforts have

been devoted for designing nanostructured electrodes with well-defined composition and morphology.<sup>20,21</sup>

Nickel foam (NF), a typical three-dimensional (3D) porous substrate with wide availability, light weight, excellent electrical conductivity, and good corrosion resistance, has attracted increasing attention as current conductors.<sup>22</sup> Various 3D Ni-based nanoarchitectures, such as NiO nanosheets,<sup>23</sup> NiO nanofibers,<sup>24</sup> Ni(OH)<sub>2</sub> nanosheets,<sup>25,26</sup> NiCo<sub>2</sub>O<sub>4</sub> nanosheets,<sup>11</sup> and Ni<sub>3</sub>FeN nanosheets,<sup>27</sup> have been grown on the NF for electrochemical energy storage and conversion. For instance, Lu and his co-workers developed a Ni@NiO electrode with an area capacitance of  $2.0 \text{ F cm}^{-2}$ .<sup>22</sup> In another study, Lu, Wu *et al.* developed a fiber-shaped Ni–Zn battery with a heterostructured Ni@NiO cathode.<sup>28</sup> However, for most Ni oxide-based electrodes, their long-term durability is still unsatisfactory, especially at high charge/discharge current densities. The development of economical, environment friendly, and feasible approaches towards high-performance Ni oxide-based electrode materials for hybrid supercapacitors and Ni–Zn batteries is highly challenging and widely pursued.

In this work, we developed a facile etching-reoxidation approach for the fabrication of a core@shell structured NF@NiO, which functions as high-performance free-standing electrodes for both hybrid supercapacitors and rechargeable Ni–Zn batteries. When applied as the cathode for hybrid supercapacitors, the as-synthesized NF@NiO achieves a high areal capacitance of  $2.01 \text{ F cm}^{-2}$  at  $8 \text{ mA cm}^{-2}$ . By coupling with an FeOOH anode, the NF@NiO//FeOOH hybrid supercapacitor demonstrates a peak energy density of  $2.15 \text{ mW h cm}^{-3}$  and a peak power density of  $2.75 \text{ W cm}^{-3}$ . The NF@NiO can also act

State Key Laboratory of Advanced Technology for Materials Synthesis and Processing, Wuhan University of Technology, Wuhan 430070, P. R. China. E-mail: liangzhou@whut.edu.cn; mlq518@whut.edu.cn

† Electronic supplementary information (ESI) available: Digital photos and HRTEM image of NF and NF@NiO, CV curves at various scan rates; GCD curves of NF; Nyquist plots collected for electrodes; SEM image of the FeOOH nanoparticles; CV and GCD curves of FeOOH; Nyquist plots collected for an NF@NiO//FeOOH device; the SEM images and GCD of the batteries after cycles. See DOI: 10.1039/c8ta07574c

as cathodes for Ni–Zn batteries. The NF@NiO//Zn battery delivers a remarkable energy density of  $25.6 \mu\text{W h cm}^{-2}$ , a peak power density of  $86.48 \text{ mW cm}^{-2}$ , and an extraordinary cycling durability (87% capacity retention for 10 000 cycles).

## Experimental

### Synthesis of NF@NiO

Before acid treatment, the compressed NF (thickness: 0.4 mm, mass per unit area:  $47.3 \text{ mg cm}^{-2}$ ) was cleaned with acetone, alcohol, HCl, and distilled water, then dried at room temperature overnight. The cleaned NF was then transferred into a solution (20 mL) containing  $\text{H}_3\text{PO}_4$  (1.00 M),  $\text{LiCl}\cdot\text{H}_2\text{O}$  (1.00 M), and  $\text{KBH}_4$  (0.05 M). The container was sealed with a cap and then heated to  $120^\circ\text{C}$  for 120 min. The samples were collected, thoroughly washed with distilled water, and dried.

### Synthesis of FeOOH nanoparticles

The FeOOH nanoparticles on carbon cloth were synthesized by hydrothermal and electrochemical activation transformation methods reported recently.<sup>29</sup>

### Fabrication of NF@NiO//FeOOH HSCs

The NF@NiO//FeOOH hybrid supercapacitors were assembled using NF@NiO ( $0.5 \text{ cm} \times 1.0 \text{ cm}$ ) as the positive electrode, FeOOH on carbon cloth ( $0.5 \text{ cm} \times 1.0 \text{ cm}$ ) as the negative electrode, and KOH (1.00 M) aqueous solution as the electrolyte.

### Fabrication of Ni–Zn batteries

The Ni–Zn batteries were assembled using NF@NiO ( $0.5 \text{ cm} \times 1.0 \text{ cm}$ ) as the positive electrode, zinc plates ( $0.5 \text{ cm} \times 1 \text{ cm}$ ) as the negative electrode, and a KOH (1.00 M) aqueous solution as the electrolyte. The quasi-solid-state Ni–Zn batteries were assembled by separating the NF@NiO cathode and Zn anode using a NKK separator (Nippon Kodoshi Corporation). PVA/KOH gel was employed as the electrolyte. The gel electrolyte was prepared by dissolving PVA (2.0 g) in distilled water (15 mL) at  $85^\circ\text{C}$  under vigorous stirring. Then, a KOH aqueous solution (4.0 M, 10 mL) was added into the well-dissolved PVA solution.

### Material characterization and electrochemical measurements

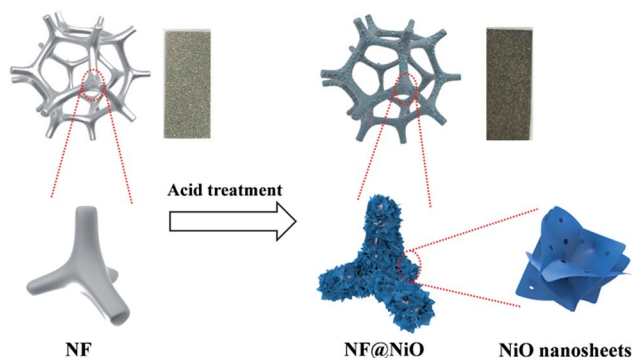
The sample compositions were analyzed using a Bruker D8 Discover X-ray diffractometer with a non-monochromatic Cu K $\alpha$  X-ray source and a Raman spectrometer (Renishaw INVIA). The morphology of the samples was studied using a field-emission SEM (JEOL-7100F) and a TEM (JEM-2100F). The valence states of Ni in the materials were tested by using an XPS (VG MultiLAB 2000). The electrochemical measurements were collected on an electrochemical workstation (CHI 760D). The supercapacitor performances were first studied in a typical three-electrode system in the KOH (1.00 M) aqueous solution. A saturated calomel electrode (SCE) was employed as the reference electrode and a carbon rod was used as the counter electrode. The electrochemical performances of the aqueous Ni–Zn batteries were determined in a two-electrode cell in a solution of KOH

(1.00 M) and  $\text{Zn}(\text{Ac})_2$  (0.02 M). The capacitive current was used to determine the electrochemical active surface areas (ECSA) of the as-prepared NF and NF@NiO with a scan window of 0.27–0.32 V *versus* SCE. The current density differences at 0.29 V against the scan rate (4 to  $16 \text{ mV s}^{-1}$ ) were fitted to obtain the double-layer capacitance ( $C_{dl}$ ) and ECSA.

## Results and discussion

The synthesis of core@shell structured NF@NiO is realized through a facile etching-reoxidation approach (Scheme 1). Typically, a piece of cleaned NF is directly immersed into an aqueous acidic solution. During the reaction process ( $120^\circ\text{C}$  for 120 min), the surface NiO and a part of the elemental Ni are dissolved in the acidic solution. The dissolution of NiO and Ni can be reflected from the colour change of the solution and the weight change of the sample (ESI, Fig. S1 $\dagger$ ). The newly exposed Ni surface is highly reactive; when it comes into contact with the  $\text{O}_2$  dissolved in the solution, it can be immediately oxidized into NiO nanosheets. The colour of the sample is darkened after the acidic treatment (Fig. S1 $\dagger$ ), indicating the formation of NiO.

The conversion of NF to core@shell structured NF@NiO is firstly investigated by scanning electron microscopy (SEM), transmission electron microscopy (TEM), selected area electron diffraction (SAED), and energy dispersive X-ray spectroscopy (EDS). The pristine NF possesses a 3D macroporous structure with a smooth surface (Fig. 1a and b). After acid treatment, the surface becomes rich in etching cracks and stripes (Fig. 1c). The high-magnification SEM image shows the full coverage of the surface with large amounts of nanosheets with a thickness of  $\sim 20 \text{ nm}$  (Fig. 1d). The TEM image reveals the mesoporous feature of the nanosheet (Fig. 1e). The HRTEM image (Fig. S2 $\dagger$ ) shows clear inter-planar spacings of 0.21 and 0.24 nm, corresponding to the (012) and (101) lattice fringes of NiO, respectively.<sup>28</sup> The SAED pattern (Fig. 1f) displays a series of concentric diffraction rings, suggesting the polycrystalline nature of the nanosheet. The diffraction rings can be indexed to the (101), (012), (110), and (104) diffractions of NiO (JCPDS no. 44-1159). Both the HRTEM image and SAED pattern demonstrate that the nanosheets are NiO rather than metallic Ni. The EDS mappings show the homogeneous spatial distribution of Ni and O (Fig. 1g), verifying the NiO composition of the nanosheets.



Scheme 1 Schematic illustration of the synthesis process of the core@shell structured NF@NiO.

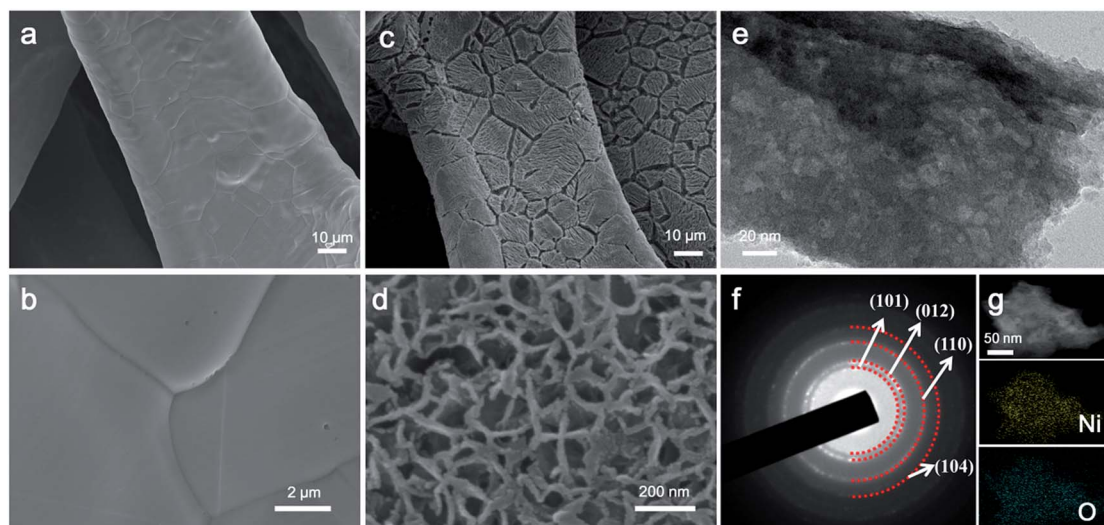


Fig. 1 (a and b) SEM images of the pristine NF at different magnifications. (c and d) SEM images of the as-prepared NF@NiO at different magnifications. (e) TEM image and (f) SAED pattern of the NiO nanosheet. (g) HAADF-STEM image of the NiO nanosheet and the corresponding elemental mapping images.

The possible phase and chemical compositions of the samples are studied by X-ray diffraction (XRD), Raman spectroscopy, and X-ray photoelectron spectroscopy (XPS). The NF and NF@NiO show almost identical XRD patterns (Fig. 2a), which can be indexed to metallic Ni (JCPDS no. 04-0850). The absence of diffraction peaks for NiO in NF@NiO suggests that the NiO shell is relatively thin. No characteristic Raman peak can be observed for NF, indicating the high-purity metallic nature of NF (Fig. 2b). In sharp contrast, the NF@NiO shows characteristic peaks at 427, 705, 1259 and 417.6  $\text{cm}^{-1}$ , corresponding to the one-phonon (1P), two-phonon (2P), and two-magnon (2M) scattering longitudinal modes of NiO.<sup>30</sup> The Raman results demonstrate that NiO is formed during the acid treatment, which can be further confirmed by XPS. The NF and NF@NiO show quite similar XPS survey spectra, except for the stronger O signal of NF@NiO (Fig. 2c). Fig. 2d compares the Ni

2p XPS core level spectra of NF and NF@NiO. The pristine NF exhibits two peaks at 855.9 and 873.8 eV, which can be ascribed to the  $2p_{3/2}$  and  $2p_{1/2}$  components of Ni(0), respectively.<sup>22,31</sup> Meanwhile, the peaks located at 852.6 ( $2p_{3/2}$ ) and 869.7 eV ( $2p_{1/2}$ ) are associated with metallic Ni.<sup>28,32</sup> Compared to the pristine NF, the NF@NiO shows much stronger Ni<sup>2+</sup> signals and much weaker Ni(0) signals, suggesting that the NF surface is oxidized during the acid treatment.

The supercapacitor performances of the pristine NF and NF@NiO are studied in a three-electrode system. KOH (1.00 M) is used as the electrolyte. The cycle voltammetry (CV) curves of NF and NF@NiO are shown in Fig. 3a and S3.† Both the NF and NF@NiO represent a pair of cathodic/anodic peaks, corresponding to the redox reaction,  $\text{NiO} + \text{OH}^- = \text{NiOOH} + \text{e}^-$ . The well-defined redox peaks suggest the typical pseudo-capacitive properties of the electrodes. The good symmetric feature of the reduction/oxidation peaks demonstrates the excellent reversibility of the redox reaction. When compared to the pristine NF, the NF@NiO demonstrates substantially higher current responses, suggesting its better pseudo-capacitive performance.

The galvanostatic charge/discharge (GCD) profiles of NF and NF@NiO at 10  $\text{mA cm}^{-2}$  are shown in Fig. 3b. Obviously, the NF@NiO demonstrates much longer discharge time than NF, suggesting its much higher capacitance. The GCD profiles of the pristine NF and NF@NiO at different current densities are presented in Fig. 3c and S4.† The NF@NiO displays an obvious discharge plateau at  $\sim 0.25$  V (vs. SCE). Considering the difficulty in determining the exact weight of electrochemically active NiO in the samples, we use area capacitance rather than specific capacitance to evaluate the supercapacitor performance. The areal capacitance of NF@NiO reaches 2.01  $\text{F cm}^{-2}$  at 8  $\text{mA cm}^{-2}$  (Fig. 3d), which is  $\sim 40$  times to NF (0.05  $\text{F cm}^{-2}$ ). Such a high areal capacitance is considerably higher than most of the NF supported free-standing electrodes reported recently, such as NF@Ni(OH)<sub>2</sub> (1.60  $\text{F cm}^{-2}$  at 2  $\text{mA cm}^{-2}$ ),<sup>33</sup> NF@CoMoO<sub>4</sub>

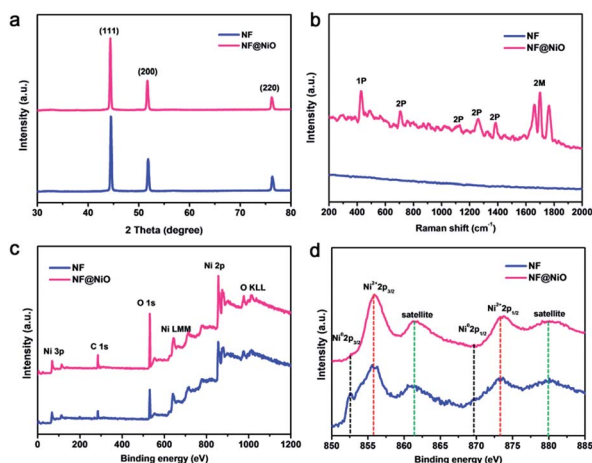


Fig. 2 (a) XRD patterns, (b) Raman spectra, (c) XPS survey spectra and (d) Ni 2p XPS spectra of NF and NF@NiO.



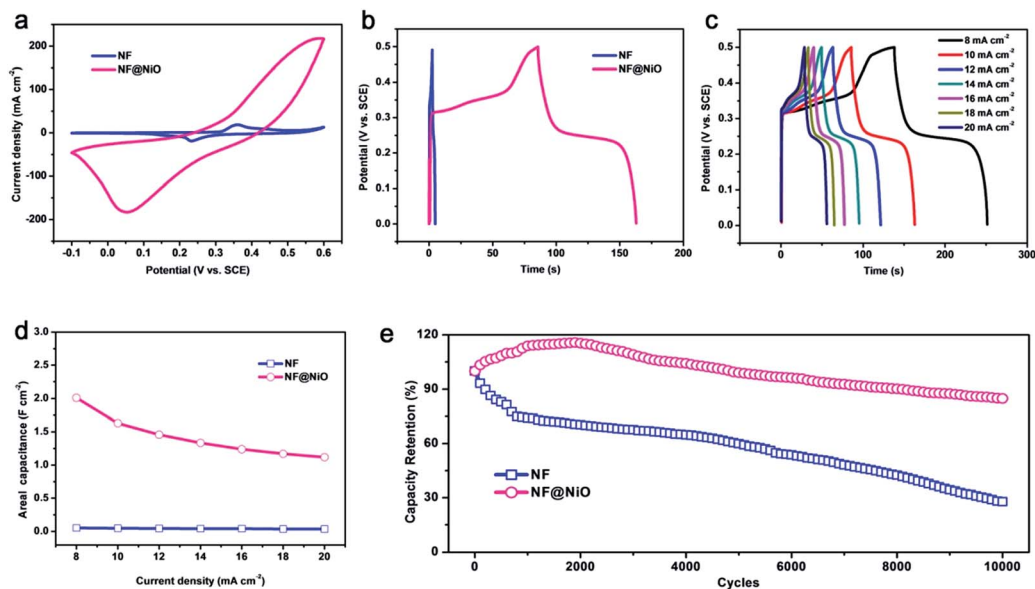


Fig. 3 (a) Cycle voltammetry (CV) curves of the NF and NF@NiO collected at  $100 \text{ mV s}^{-1}$ . (b) Galvanostatic charge/discharge (GCD) curves of the NF and NF@NiO at a current density of  $10 \text{ mA cm}^{-2}$ . (c) GCD curves of NF@NiO collected at different currents. (d) Areal capacitance as a function of the current density of the NF and NF@NiO. (e) Cycling performances of the NF and NF@NiO at  $10 \text{ mA cm}^{-2}$ .

( $1.26 \text{ F cm}^{-2}$  at  $4 \text{ mA cm}^{-2}$ ),<sup>34</sup> NF@NiCo<sub>2</sub>O<sub>4</sub> ( $1.50 \text{ F cm}^{-2}$  at  $5 \text{ mA cm}^{-2}$ ),<sup>35</sup> NF@NiCo<sub>2</sub>O<sub>4</sub>@MnO<sub>2</sub> ( $1.91 \text{ F cm}^{-2}$  at  $8 \text{ mA cm}^{-2}$ ),<sup>36</sup> and NF@CoO ( $1.23 \text{ F cm}^{-2}$  at  $1 \text{ mA cm}^{-2}$ ).<sup>37</sup> The NF@NiO also delivers an impressive rate capability. Around 61.7% of the initial capacitance can be retained with the increase of the current density from 8 to  $20 \text{ mA cm}^{-2}$ . The long-term cycling performance of NF@NiO is also studied. Interestingly, the capacitance of NF@NiO increases  $\sim 15\%$  in the first 2000 cycles, which can be attributed to the continuous oxidation and activation of the NF@NiO surface during the charging and discharging processes.<sup>22</sup> After 10 000 cycles at  $10 \text{ mA cm}^{-2}$ , the NF@NiO demonstrates an excellent capacitance retention of 84.8% (Fig. 3e). Under the same current density, the capacitance retention for the pristine NF is substantially lower (27.8%).

For comparison, the etching time is tuned from 30 to 180 min. Generally, the NiO thickness increases with the etching time (Fig. S5,† 1c and d). When employed in supercapacitors, the specific capacitance increases with etching time (NiO thickness) and reaches a maximum value of  $1.63 \text{ F cm}^{-2}$  at an etching time of 120 min (Fig. S6†). Further increase of the etching time to 180 min leads to the decrease in the capacitance ( $0.77 \text{ F cm}^{-2}$ ).

To explore the reasons for the enhanced capacitance of NF@NiO, the electrochemical active surface area is further determined through capacitance measurements. As shown in Fig. S7 and S8,† the calculated capacitances for NF@NiO and NF are 334 and  $56 \text{ mF cm}^{-2}$ , respectively. Electrochemical impedance spectroscopy (EIS) is further employed to provide more details on the electrochemical properties (Fig. S9†). The NF@NiO shows slightly a larger charge transfer resistance ( $5.06 \Omega$ ) than pristine ( $0.2 \Omega$ ), which is caused by the formation of a less conductive NiO shell at the NF surface during acid treatment. Obviously, the larger charge transfer resistance of

NF@NiO cannot lead to an improvement in the capacitance. Therefore, the enhanced supercapacitor performance of NF@NiO can be ascribed to the increased amounts of electrochemically active NiO.

To further evaluate the potential of the free-standing NF@NiO in hybrid supercapacitors, an HSC is assembled using the as-prepared NF@NiO as the cathode and an FeOOH anode. The FeOOH grown on carbon cloth is prepared by a hydrothermal method followed by electrochemical activation.<sup>29</sup> The microstructure and electrochemical performances of FeOOH are presented in Fig. S11 and S13.† Before assembly, the charges stored in the NF@NiO cathode and FeOOH anode are balanced, and the areal capacitance ratio of FeOOH to NF@NiO at  $100 \text{ mV s}^{-1}$  is 1.03 : 1 (see the ESI and Fig. S10†). CV curves at various scan rates show obvious redox peaks, suggesting the pseudo-capacitive properties of the as-fabricated NF@NiO//FeOOH HSCs (Fig. 4a). The GCD profiles of the NF@NiO//FeOOH HSCs are relatively symmetric (Fig. 4b), indicating the good reversibility of the HSCs. The volumetric capacitance of the NF@NiO//FeOOH HSCs as a function of current density is shown in Fig. 4c. The NF@NiO//FeOOH HSCs deliver a capacitance of  $5.27 \text{ F cm}^{-3}$  at  $8 \text{ mA cm}^{-2}$ . Increasing the current density doesn't cause an obvious capacitance decrease, proving the outstanding rate performance of the NF@NiO//FeOOH HSCs. Besides the high capacitance and outstanding rate performance, the NF@NiO//FeOOH HSCs also present an excellent long-term cycling performance; more than 84.7% of the initial capacitance can be retained after 5000 cycles (Fig. 4d).

The morphology and surface chemical composition of NF@NiO after cycling are characterized by SEM (Fig. S15†) and XPS (Fig. S16†). As shown in Fig. S15 and S16,† negligible change in the morphology or valence state can be observed after 5000 cycles. Fig. S17† presents the Nyquist plot of the as-

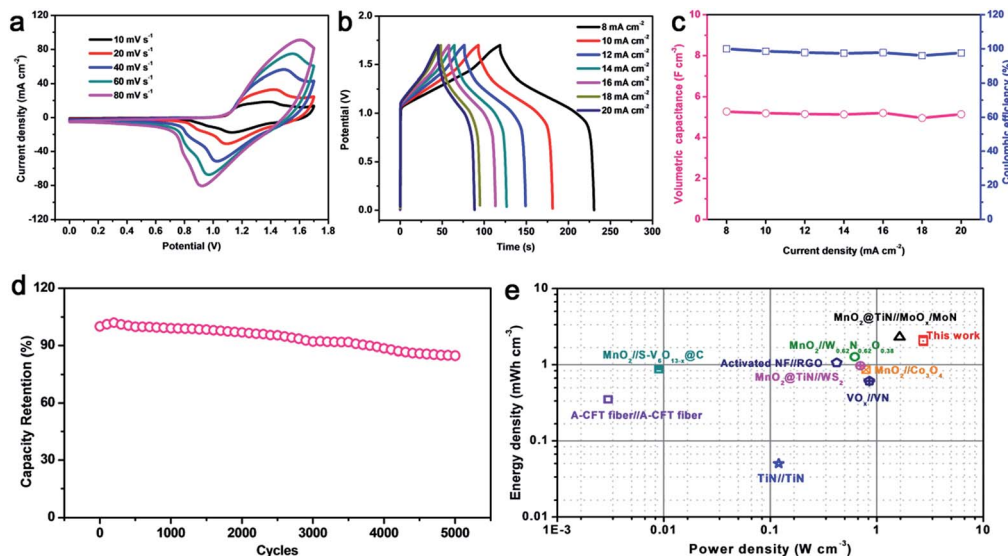


Fig. 4 (a) CV curves of the NF@NiO//FeOOH HSCs collected at various scan rates. (b) GCD curves of the compressed NF@NiO//FeOOH HSCs collected at different current densities operated within a voltage window of 1.7 V. (c) Volumetric capacitance and coulombic efficiency of the NF@NiO//FeOOH HSCs as a function of current density. (d) Cycling performance of the NF@NiO//FeOOH HSCs at  $10 \text{ mA cm}^{-2}$ . (e) Ragone plots of the NF@NiO//FeOOH HSCs. The values reported for other supercapacitors (SCs) are added for comparison.

fabricated NF@NiO//FeOOH HSCs. The NF@NiO//FeOOH HSCs show a small charge-transfer resistance ( $0.62 \Omega$ ), indicating their fast charge transfer properties.

Fig. 4e compares the volumetric power/energy densities of the NF@NiO//FeOOH HSCs with the recently reported literature values. The peak volumetric energy density of the NF@NiO//FeOOH HSCs reaches  $2.15 \text{ mW h cm}^{-3}$ . Such an energy density is higher than most of the recently developed symmetric and asymmetric supercapacitors,<sup>38–40</sup> such as activated NF/RGO ( $1.06 \text{ mW h cm}^{-3}$ ),<sup>22</sup>  $\text{VO}_x/\text{VN}$  ( $0.61 \text{ mW h cm}^{-3}$ ),<sup>41</sup>  $\text{TiN}/\text{TiN}$  ( $0.05 \text{ mW h cm}^{-3}$ ),<sup>42</sup>  $\text{MnO}_2/\text{TiN}/\text{WS}_2$  ( $0.97 \text{ mW h cm}^{-3}$ ),<sup>43</sup>  $\text{MnO}_2/\text{Co}_3\text{O}_4$  ( $0.86 \text{ mW h cm}^{-3}$ )<sup>44</sup> and  $\text{MnO}_2/\text{W}_{0.62}\text{N}_{0.62}\text{O}_{0.38}$  ( $1.27 \text{ mW h cm}^{-3}$ ).<sup>45</sup> Moreover, the maximum power density ( $2.75 \text{ W cm}^{-3}$ ) delivered by the NF@NiO//FeOOH HSCs is also much higher than most of the recently reported HSCs.

To evaluate the potential of NF@NiO for the Ni–Zn batteries, aqueous Ni–Zn batteries are assembled (denoted as NF@NiO//Zn) using Zn plates as the anode and NF@NiO as the cathode. Compared to the NF//Zn battery, the NF@NiO//Zn battery delivers a much lower voltage hysteresis and longer discharge plateaus (Fig. 5a), suggesting its less polarization and higher capacity. The discharge profiles of the NF@NiO//Zn battery exhibit a volumetric capacity of  $3200 \mu\text{A h cm}^{-3}$  at  $8 \text{ mA cm}^{-2}$ . The discharge profiles of the NF@NiO//Zn batteries manifest an operating voltage of 1.7–1.8 V at various current densities (Fig. S18†). The NF@NiO//Zn battery delivers a volumetric capacity of  $3200 \mu\text{A h cm}^{-3}$  at  $8 \text{ mA cm}^{-2}$ . Even the current density is increased to  $20 \text{ mA cm}^{-2}$ , a capacity of  $979 \mu\text{A h cm}^{-3}$  can be retained (Fig. 5b). In contrast, the NF//Zn battery delivers a much lower volumetric capacity of  $55.5 \mu\text{A h cm}^{-3}$  at  $20 \text{ mA cm}^{-2}$ . More importantly, the NF@NiO//Zn battery affords an excellent long-term cyclability. More than 87% of the capacity can be retained after 10 000 cycles at  $20 \text{ mA cm}^{-2}$ , much higher

than that of the NF//Zn battery (61.6%) (Fig. 5c). Fig. S19† presents the discharge profiles of the 1<sup>st</sup> and 10 000<sup>th</sup> cycles. As expected, there is a little change in the curve shape, which further proves the excellent cycling performance.

The energy/power densities of the fabricated NF@NiO//Zn battery are compared with the previously reported values (Fig. 5d). The NF@NiO//Zn battery delivers a remarkable power density of  $86.48 \text{ mW cm}^{-2}$ . Meanwhile, the peak energy density reaches  $25.6 \mu\text{W h cm}^{-2}$ , which is substantially higher than that

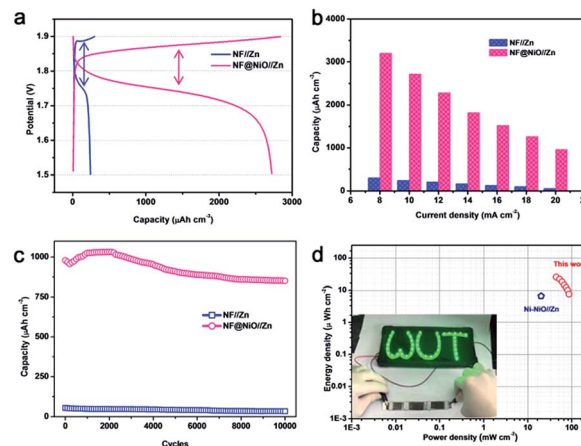


Fig. 5 (a) Charge–discharge curves of the NF//Zn and NF@NiO//Zn batteries at  $10 \text{ mA cm}^{-2}$ . (b) Volumetric capacity of the NF//Zn and NF@NiO//Zn batteries as a function of current density obtained from the galvanostatic charge/discharge curves. (c) Cycling performance of the NF//Zn and NF@NiO//Zn batteries collected at  $20 \text{ mA cm}^{-2}$ . (d) Ragone plot showing the energy density and power density of the NF@NiO//Zn battery. The inset is a neon sign consisting of 42 light-emitting diodes powered by three quasi-solid-state NF@NiO//Zn batteries in series.

of the fiber-shaped Ni@NiO//Zn ( $6.6 \mu\text{W h cm}^{-2}$ ) battery.<sup>28</sup> To exemplify the practical application of the NF@NiO//Zn batteries, three quasi-solid-state NF@NiO//Zn batteries are connected in series to power a neon sign consisting of 42 light emitting diodes (LEDs) (inset in Fig. 5d), suggesting the promising application of the NF@NiO//Zn batteries in wearable electronics.

The excellent electrochemical performances of NF@NiO can be ascribed to the following reasons. (I) The Ni foam with a macroporous architecture and excellent conductivity provides an efficient electron transfer and electrolyte accessibility. (II) The direct growth of electrochemically active NiO nanosheets on Ni foam effectively enhances the interfacial charge transfer. (III) The highly porous NiO nanosheets significantly increase the accessible active sites for redox reactions.

## Conclusions

In conclusion, an efficient etching-reoxidation method has been demonstrated to produce high-performance free-standing NF@NiO core@shell electrodes for hybrid supercapacitors and rechargeable Ni–Zn batteries. The direct growth of NiO nanosheets on Ni foam significantly improves not only the activity but also the kinetics. When compared to the pristine NF ( $0.05 \text{ F cm}^{-2}$ ), an up to fortyfold enhancement in the areal capacitance can be achieved for NF@NiO ( $2.01 \text{ F cm}^{-2}$ ). The fabricated NF@NiO//FeOOH HSCs demonstrate a peak energy density of  $2.15 \text{ mW h cm}^{-3}$  at a power density of  $2.73 \text{ W cm}^{-3}$ . The NF@NiO//Zn battery manifested a high peak energy density ( $25.6 \mu\text{W h cm}^{-2}$ ) and an impressive power density ( $86.48 \text{ mW cm}^{-2}$ ) with excellent cycling durability (87% capacity retention for 10 000 cycles). The excellent supercapacitor and Ni–Zn battery performances render the free-standing NF@NiO an attractive candidate for electrochemical energy storage.

## Conflicts of interest

There are no conflicts to declare.

## Acknowledgements

This work was supported by the National Key Research and development program of China (2016YFA0202603), the National Natural Science Foundation of China (21673171, 51502226), the Programme of Introducing Talents of Discipline to Universities (B17034), the National Natural Science Fund for Distinguished Young Scholars (51425204).

## Notes and references

- M. F. El-Kady, S. Veronica, D. Sergey and R. B. Kaner, *Science*, 2012, **335**, 1326–1330.
- J. Liu, K. Song, P. A. V. Aken, J. Maier and Y. Yu, *Nano Lett.*, 2014, **14**, 2597–2603.
- J. Bae, M. K. Song, Y. J. Park, J. M. Kim, M. Liu and Z. L. Wang, *Angew. Chem., Int. Ed.*, 2011, **50**, 1683–1687.
- Z. Teng, L. Wan, S. Sun, C. Qi, S. Jiao, Q. Xia and X. Hui, *Adv. Mater.*, 2017, **29**, 1604167.
- H. Pang, X. Li, Q. Zhao, H. Xue, W. Y. Lai, Z. Hu and W. Huang, *Nano Energy*, 2017, **35**, 138–145.
- K. Naoi, K. Kisu, E. Iwama, S. Nakashima, Y. Sakai, Y. Orikasa, P. Leone, N. Dupré, T. Brousse and P. Rozier, *Energy Environ. Sci.*, 2016, **9**, 2143–2151.
- L. Zhou, K. Zhang, J. Sheng, Q. An, Z. Tao, Y. M. Kang, J. Chen and L. Mai, *Nano Energy*, 2017, **35**, 281–289.
- X. Xu, H. Song, S. Lin, Z. Ying, X. Zhan, Z. Hu, Z. Qi, J. Sun, Y. Bo and T. Li, *Nat. Commun.*, 2016, **7**, 11296.
- B. Li, P. Gu, Y. Feng, G. Zhang, K. Huang, H. Xue and H. Pang, *Adv. Funct. Mater.*, 2017, **27**, 1605784.
- H. Lai, Q. Wu, J. Zhao, L. Shang, H. Li, R. Che, L. Zhiyang, J. Xiong, L. Yang and X. Wang, *Energy Environ. Sci.*, 2016, **9**, 2053–2060.
- G. Zhang and X. W. Lou, *Adv. Mater.*, 2013, **25**, 976–979.
- G. Meng, Q. Yang, X. Wu, P. Wan, Y. Li, X. Lei, X. Sun and J. Liu, *Nano Energy*, 2016, **30**, 831–839.
- Y. Liu, J. Li, F. Li, W. Li, H. Yang, X. Zhang, Y. Liu and J. Ma, *J. Mater. Chem. A*, 2016, **4**, 4472–4478.
- M. Ma, J. P. Tu, Y. F. Yuan, X. L. Wang, K. F. Li, F. Mao and Z. Y. Zeng, *J. Power Sources*, 2008, **179**, 395–400.
- F. Beck and P. Rüetschi, *Electrochim. Acta*, 2000, **45**, 2467–2482.
- M. Gong, Y. Li, H. Zhang, B. Zhang, W. Zhou, J. Feng, H. Wang, Y. Liang, Z. Fan and J. Liu, *Energy Environ. Sci.*, 2014, **7**, 2025–2032.
- H. Kim, G. Jeong, Y. U. Kim, J. H. Kim, C. M. Park and H. J. Sohn, *Chem. Soc. Rev.*, 2013, **42**, 9011–9034.
- C. Xu, J. Liao, C. Yang, R. Wang, D. Wu, P. Zou, Z. Lin, B. Li, F. Kang and C. P. Wong, *Nano Energy*, 2016, **30**, 900–908.
- M. M. Sk, C. Y. Yue, K. Ghosh and R. K. Jena, *J. Power Sources*, 2016, **308**, 121–140.
- P. Hu, T. Wang, J. Zhao, C. Zhang, J. Ma, H. Du, X. Wang and G. Cui, *ACS Appl. Mater. Interfaces*, 2015, **7**, 26396–26399.
- Z. Lu, X. Wu, X. Lei, Y. Li and X. Sun, *Inorg. Chem. Front.*, 2015, **2**, 184–187.
- M. Yu, W. Wang, C. Li, T. Zhai, X. Lu and Y. Tong, *NPG Asia Mater.*, 2014, **6**, e129.
- M. Huang, F. Li, J. Y. Ji, Y. X. Zhang, X. L. Zhao and X. Gao, *CrystEngComm*, 2014, **16**, 2878–2884.
- M. Kundu and L. Liu, *Mater. Lett.*, 2015, **144**, 114–118.
- H. Wang, Y. Liang, T. Mirfakhrai, Z. Chen, H. S. Casalongue and H. Dai, *Nano Res.*, 2011, **4**, 729–736.
- X. Xiong, D. Ding, D. Chen, G. Waller, Y. Bu, Z. Wang and M. Liu, *Nano Energy*, 2015, **11**, 154–161.
- B. Zhang, C. Xiao, S. Xie, J. Liang, X. Chen and Y. Tang, *Chem. Mater.*, 2016, **28**, 6934–6941.
- Y. Zeng, Y. Meng, Z. Lai, X. Zhang, M. Yu, P. Fang, M. Wu, Y. Tong and X. Lu, *Adv. Mater.*, 2017, **29**, 1702698.
- K. A. Owusu, L. Qu, J. Li, Z. Wang, K. Zhao, C. Yang, K. M. Hercule, C. Lin, C. Shi and Q. Wei, *Nat. Commun.*, 2017, **8**, 14264.
- N. Mironovaulmane, A. Kuzmin, I. Steins, J. Grabis, I. Sildos and M. Pärns, *J. Phys.: Conf. Ser.*, 2007, **93**, 012039.
- Y. Li, X. Li, Z. Wang, H. Guo and T. Li, *Ceram. Int.*, 2016, **42**, 14565–14572.

- 32 T. Hou, L. Yuan, T. Ye, L. Gong, J. Tu, M. Yamamoto, Y. Torimoto and Q. Li, *Int. J. Hydrogen Energy*, 2009, **34**, 9095–9107.
- 33 Y. F. Yuan, X. H. Xia, J. B. Wu, J. L. Yang, Y. B. Chen and S. Y. Guo, *Electrochim. Acta*, 2012, **56**, 2627–2632.
- 34 D. Guo, H. Zhang, X. Yu, M. Zhang, P. Zhang, Q. Li and T. Wang, *J. Mater. Chem. A*, 2013, **1**, 7247–7254.
- 35 L. Yu, G. Zhang, C. Yuan and X. W. Lou, *Chem. Commun.*, 2013, **49**, 137–139.
- 36 K. Xu, W. Li, Q. Liu, B. Li, X. Liu, L. An, Z. Chen, R. Zou and J. Hu, *J. Mater. Chem. A*, 2014, **2**, 4795–4802.
- 37 C. Zhou, Y. Zhang, Y. Li and J. Liu, *Nano Lett.*, 2013, **13**, 2078–2085.
- 38 M. Yu, X. Cheng, Y. Zeng, Z. Wang, Y. Tong, X. Lu and S. Yang, *Angew. Chem., Int. Ed.*, 2016, **55**, 6762–6766.
- 39 Y. Huang, H. Hu, Y. Huang, M. Zhu, W. Meng, C. Liu, Z. Pei, C. Hao, Z. Wang and C. Zhi, *ACS Nano*, 2015, **9**, 4766–4775.
- 40 T. Zhai, X. Lu, Y. Ling, M. Yu, G. Wang, T. Liu, C. Liang, Y. Tong and Y. Li, *Adv. Mater.*, 2014, **26**, 5869–5875.
- 41 X. Lu, M. Yu, T. Zhai, G. Wang, S. Xie, T. Liu, C. Liang, Y. Tong and Y. Li, *Nano Lett.*, 2013, **13**, 2628–2633.
- 42 X. Lu, G. Wang, T. Zhai, M. Yu, S. Xie, Y. Ling, C. Liang, Y. Tong and Y. Li, *Nano Lett.*, 2012, **12**, 5376–5381.
- 43 S. Liu, Y. Zeng, M. Zhang, S. Xie, Y. Tong, F. Cheng and X. Lu, *J. Mater. Chem. A*, 2017, **5**, 21460–21466.
- 44 W. Xu, J. Chen, M. Yu, Y. Zeng, Y. Long, X. Lu and Y. Tong, *J. Mater. Chem. A*, 2016, **4**, 10779–10785.
- 45 M. Yu, Y. Han, X. Cheng, L. Hu, Y. Zeng, M. Chen, F. Cheng, X. Lu and Y. Tong, *Adv. Mater.*, 2015, **27**, 3085–3091.